



OpenFOAM based LES of slot jet impingement heat transfer at low nozzle to plate spacing using four SGS models

Anuj Kumar Shukla¹ · Anupam Dewan¹

Received: 14 March 2018 / Accepted: 28 August 2018 / Published online: 7 September 2018
© Springer-Verlag GmbH Germany, part of Springer Nature 2018

Abstract

The objective of the present investigation is to assess the effectiveness of large eddy simulation (LES) in turbulent slot jet impingement heat transfer at low nozzle to plate spacing. Four different sub-grid stress (SGS) models, namely, Smagorinsky, WALE (wall adapting local eddy-viscosity), k -equation and dynamic k -equation, were considered for Reynolds number of 20,000. Computations were performed using OpenFOAM, an open source finite-volume based CFD code. Time and span-wise averaged mean streamwise velocity and root mean square (r.m.s.) velocity fluctuations in the stagnation and wall jet regions are presented. Nusselt number distributions on the impingement wall are also presented. The computed LES results are compared with the reported experimental data. A secondary peak in the Nusselt number was observed using the four SGS models as in the experimental data. LES of slot jet impingement heat transfer using four SGS models, including WALE, has been investigated for the first time in the present paper. It is observed that the WALE and dynamic k -equation SGS models perform well in complex flow regions of turbulent slot jet impingement heat transfer.

Keywords Jet Impingement · LES · WALE · Heat Transfer · Turbulence · Nusselt Number

Nomenclature

B	Slot width
e	Internal energy
h	Heat transfer coefficient (W/m^2-K)
H	Height between nozzle to plate
H/B	Normalized nozzle to plate spacing
Re	Reynolds number ($\rho UB/\mu$)
k	Turbulence kinetic energy
k_a	Thermal conductivity ($W/m-K$)
k_{SGS}	Sub-grid scale turbulence kinetic energy
Nu	Nusselt number (hB/k)
P	Mean pressure
Pr	Prandtl number
q_{tk}	Turbulent heat flux
S	STRAIN rate tensor
T	Sub-grid stress tensor
T	Mean temperature

t^*	Non dimensional time unit
U	Mean velocity
u'	r.m.s. streamwise velocity fluctuation
V_o	Velocity at jet inlet
x,y,z	Coordinate directions
Ω	Vorticity magnitude
ε_{SGS}	Sub-grid scale dissipation
ν_{SGS}	Sub-grid scale kinematic viscosity
Δ	Grid size
μ	Dynamic viscosity ($kg/s-m$)

Subscript

i, j, k	Index notation
0	Quantities at the inlet
SGS	Sub-grid scale
eff	Effective
t	Turbulent
a	Air
st	Stagnation

✉ Anupam Dewan
adedwan@am.iitd.ac.in

¹ Department of Applied Mechanics, Indian Institute of Technology Delhi, Hauz Khas, New Delhi 110016, India

Superscript

+ Normalized quantity in wall coordinates

1 Introduction

Jet impingements on heated surfaces are used to enhance heat transfer and it is one of the most widely employed configurations among the conventional methods for cooling or heat removal processes [1]. Variation in turbulence kinetic energy, thus turbulence intensity or normal velocity gradient, in the vicinity of an impingement surface affects heat transfer rate [2]. Hence a thorough investigation of turbulence kinetic energy and velocity distribution near the impingement wall is an important, but a computationally challenging task, for jet impingement heat transfer. Several applications of impinging jets for efficiency and safety of industrial needs are encountered, such as, road safety (effective removal of ice from roads), cooling of internal surfaces of gas turbine blades, cooling of outer combustor walls and glass manufacturing, etc.

Jet impingement heat transfer finds important considerations by researchers because of its highest heat transfer rate among all single-phase arrangements as well as its applied and fundamental significance [1]. Several studies dealing with jet impingement heat transfer have been reported experimentally and computationally [3–12]. Some researchers considered low nozzle to plate spacing for jet impingement on a heated surface experimentally and computationally [3–10]. A secondary peak in the profile of Nusselt number on impingement plate appears in the horizontal direction for a low nozzle to plate spacing [3]. The potential core length can be observed to be nearly 4.7–7.7 times the slot width from the jet exit and a free-jet region may not appear if the impingement plate is kept within a distance of two slot widths (B) from the jet exit [2]. Some parameters that affect the flow and heat transfer features are, jet to plate gap (H/B), Reynolds number (Re) and turbulence at the jet exit. Figure 1 (a) shows different regions associated with jet impingement on a flat surface and Fig. 1b shows typical Kolmogorov energy spectrum in a turbulent flow. Results on effects of these parameters may be found in several studies [2–12]. Researches have carried out computational investigation of such configurations by means of Reynolds-averaged Navier-Stokes (RANS) modelling, large eddy simulation (LES), direct numerical simulation (DNS) and hybrid computational modelling, such as, PANS (Partial-Averaged Navier-Stokes) and DES (detached eddy simulation), etc. [8–20]. A RANS computation involves solution of the time-averaged Navier-Stokes equations and the largest scales are modelled with the help of suitable turbulence models. In DNS, instantaneous 3-D Navier-Stokes equations are solved without any modelling. LES involves solution of the filtered Navier-Stokes equations by resolving scales from domain size down to the filter size (Δ), so that a considerable portion of high wave number eddy fluctuations are resolved (Fig. 1b). With advancements in computational resources in the recent decades, DNS and LES have become important and these can be used to investigate instantaneous, 3-D turbulent flow structures.

However DNS is still limited to low values of Re and therefore LES computations are preferred in practical situations [2].

Jet impingement heat transfer is a complex flow configuration with the presence of free jet, stagnation and wall jet regions involving strong streamline curvature and pressure gradient, and therefore its computation is a challenging task [2, 9, 13–20]. It is important to assess the accuracy of RANS, LES or hybrid modelling computations by comparing computed results with the experimental data for this flow configuration. This flow configuration becomes complicated with an increase in value of Re . With the limitations of experimental techniques, computational methods need to be assessed for their efficacy to simulate such type of complex flows.

Few researchers performed RANS simulations and observed that none of the RANS models based calculations were able to compute impinging jet heat transfer with a desirable accuracy [1, 2, 9–12, 21]. Thus for jet impingement heat transfer higher order solution methodologies, such as, DNS, LES and hybrid computational models, need to be assessed. Some researchers employed DNS, LES and hybrid modelling approaches and showed that the predictions with these methods were in reasonable accuracy [15–20, 22–26]. LES results [8, 15–19, 24–27] were within the accepted accuracy limits. Dutta et al. [8], Olson and Fuchs [15] and Lodato et al. [26] considered different SGS models and reported accuracies obtained using different SGS models for jet impingement heat transfer. Lodato et al. [26] compared standard WALE and Lagrangian dynamic Smagorinsky models for round jet impingement with Re of 23,000 and 70,000. They studied wall jet interaction and observed that the WALE model performed satisfactorily with an improved prediction of the second-order moments. Dairy et al. [27] performed LES for turbulent round jet impingement for a low jet to plate spacing ($H/D = 2$) with the dynamic Smagorinsky and WALE models. They reported that these models produced numerical error at small scales and thus inaccurate heat transfer predictions were observed in the impingement region.

Uddin et al. [24] performed LES with the dynamic Smagorinsky model and second-order accurate discretization schemes in time and space. They observed that LES computations for jet impingement produced reasonable results that were quite sensitive to grid selections in different regions. Dairy et al. [27] performed LES and DNS for jet impingement on a heated plate. They considered two LES formulations, i.e., one with higher order schemes and other based on the conventional eddy viscosity, and compared the results with their DNS data. They observed that both the LES formulations performed well in the prediction of velocity statistics. They also observed unrealistic heat transfer prediction with the dynamic Smagorinsky and WALE SGS models due to strong nonlinearities in their mathematical formulations. Kubacki and Dick [20] considered hybrid computational models as well as LES. They considered the spanwise domain size equal to $11B$ and

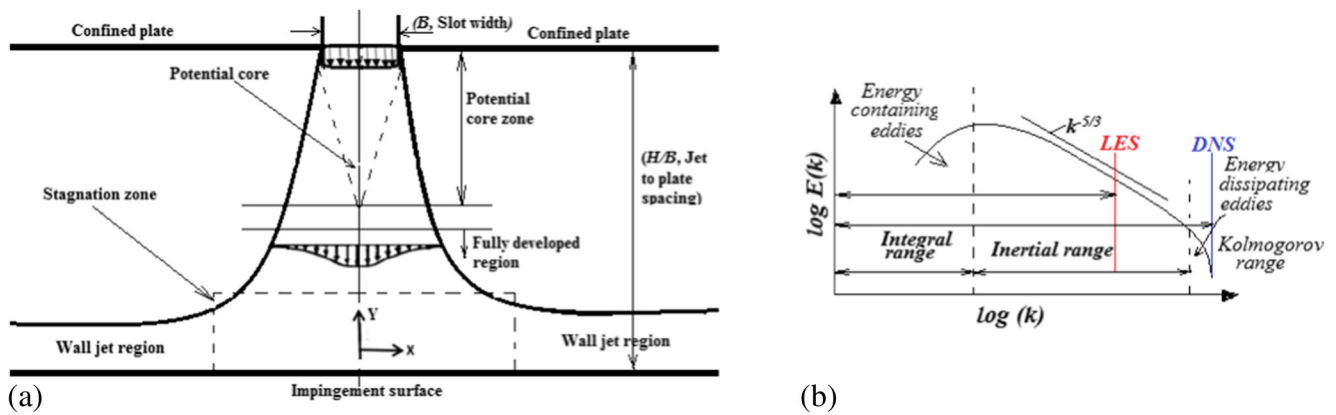


Fig. 1 a Different regions associated to jet impingement, b Kolmogorov energy spectrum

considered periodic boundary conditions in this direction. They showed that hybrid models provided reasonable accuracy compared to RANS models and former may be appropriate for impinging jet calculations. Many researchers considered periodic boundary conditions in the spanwise direction in their LES computations and the length of the domain in this direction were selected in the range of $2B - 4B$ for different jet to plate spacings (H/B) [8, 16–18, 20].

It can be observed from the above-mentioned literature review that LES is fairly accurate when applied to jet impingement heat transfer. Further an extremely small number of studies have been reported on LES of a slot jet impingement heat transfer. It can also be observed that no study on mean and turbulence characteristics along the wall jet region for a slot jet impingement using LES has been reported. In the present study four LES subgrid models, namely, Smagorinsky, WALE (wall adapting local eddy-viscosity), k -equation and dynamic k -equation, have been used to compute characteristics of impinging jet heat transfer using OpenFOAM 4.1, an open source CFD software. Profiles of mean and turbulence quantities are presented and validated at several locations in the horizontal direction $1 \leq x/B \leq 9$. The present region of interest covers the stagnation zone and wall jet development region. Profiles of Nusselt number obtained by all four SGS models are also studied and compared with the reported experimental data. Detailed comparisons of mean and turbulent quantities with the reported experimental results [3, 6] are also performed. Section 2 provides details of flow configuration and boundary conditions followed by Section 3 which deals with mathematical formulation and computational methodology. Section 4 provides numerical strategy and Section 5 results and discussions.

2 Computational domain, boundary conditions and meshing strategy

Figure 2 shows the 3-D computational domain, boundary conditions and details of grid. The computational domain

comprised of inflow at the nozzle inlet where almost a flat mean velocity V_0 was specified based on the value of Re and slot width, $Re = V_0 B / \nu$ (here B denotes the slot width and ν (m^2/s) the kinematic viscosity). A turbulent intensity of 1% similar to that taken by Ashforth-Frost et al. [3] and 0.9% taken by Zhe and Modi [6] with a turbulent length scale of $0.015B$ similar to Ashforth-Frost et al. [3] was provided. The outflow conditions were applied at the outlet. The outlet was kept at sufficiently large distance from the nozzle center line ($x/B = \pm 4.5B$) to avoid a backflow. A wall confinement was provided on the slot edges on both sides of jet and it was assumed to be adiabatic with no-slip condition. Periodic boundary conditions were applied in the spanwise direction at a distance of $Z = 11B$. The impingement plate was maintained at a constant temperature of 320 K with no slip condition. The no slip boundary conditions were applied at all the walls including for the unresolved fluctuations of velocity u'_i , for which $k_{SGS} = 0$ everywhere at the wall. Table 1 summarizes the boundary conditions used at the walls.

Two different mesh sizes named $M1$ and $M2$ were considered, where $M1$ is a fine grid with a grid size of 16,268,000 with $y^+ \sim 1$ at the first grid points next to the impingement surface and $M2$ with a grid size of 8,228,000 with $y^+ \sim 5$ at the first grid points. Minimum values of $\Delta x^+ = 30$ and $\Delta z^+ = 50$ were maintained near the impingement region based on the maximum friction velocity. A non-uniform mesh was used in the present study and grids were made finer at critical locations where the flow physics were expected to be complex in nature, such as, near the impingement surface, stagnation region, jet centerline and wall jet regions, etc. (Fig. 2).

3 Mathematical formulation and computational methodology

Turbulence involves formation of eddies and their breakdown into smaller eddies, i.e., it contains a wide range of scales.

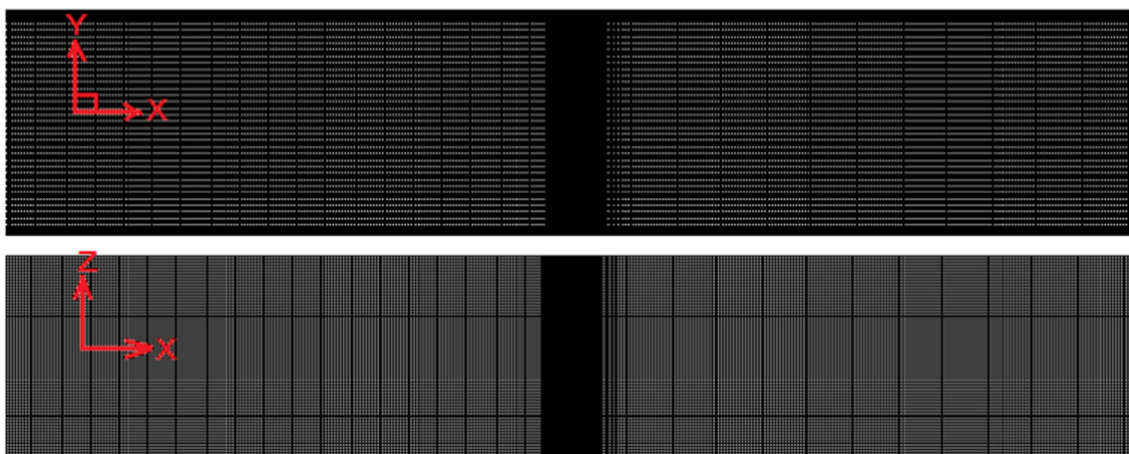
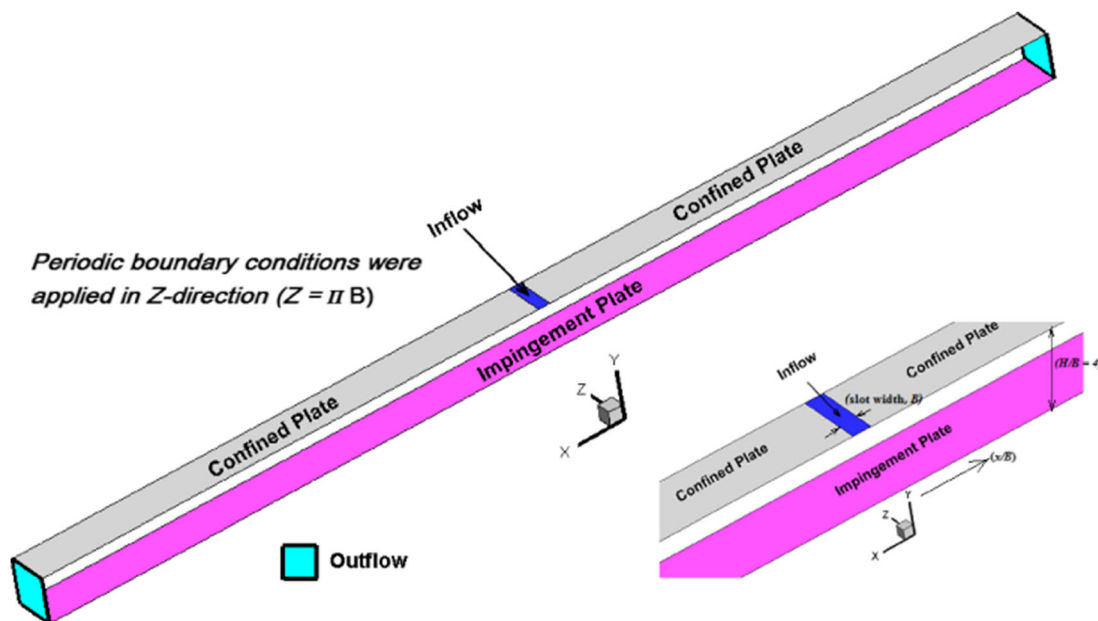


Fig. 2 Computational domain, boundary condition and non-uniform grid

The process of energy cascade occurs from large, unstable eddies to smaller eddies, which are somewhat isotropic in nature. Figure 1b shows an energy spectrum using the Kolmogorov theory. LES involves numerical solution to capture evolution of large scales. Hence those eddies which have length scales larger than a particular scale Δ measured with the computational grids are considered for direct computation, i.e., without any modelling (Fig. 2). The cutoff length is accomplished with the help of a cutoff filter between the larger and smaller scales, referred as the grid size for an implicitly filtered LES. In LES a filtering operation is performed via mathematical operation (convolution operation) for separation of turbulent length scales. It is stated as a convolution of appropriate flow field with a chosen filter kernel defined as

$$\bar{\varnothing}(x, t) = \iiint_{-\infty}^{\infty} \varnothing(x, t) G(x-\xi, \Delta) d^3 \xi \tag{1}$$

where G denotes kernel, \varnothing the flow variable and Δ the cut-off width of the filter that is responsible for the filtering of scales. In the present study over-bar is used to show a filtered variable

Table 1 Boundary conditions at the walls

Field	Type	Value
\bar{u}_i	Dirichlet	0
k_{SGS}	Dirichlet	0
p	Von Neumann	0

Table 2 Transport properties of air

Property	Value
Density (ρ)	1.225 (kg/m ³)
Kinematic viscosity (ν)	1.46×10^{-5} (m ² /s)
Thermal conductivity (k)	0.0242 (W/m-K)
Prandtl number	0.74
Air inlet temperature	300 (K)

$$\varnothing(x, t) = \bar{\varnothing}(x, t) + \varnothing'(x, t) \quad (2)$$

where $\varnothing(x, t)$ denotes the instantaneous flow property, $\bar{\varnothing}(x, t)$ its filtered (resolved) component and $\varnothing'(x, t)$ its unresolved (modeled) component, which is left out after the filtering operation. All the unresolved parts of the length scales are usually referred to as the subgrid scales (SGS). In the present study since the grid is being used as a filter it is called a box filter. The physical sense of convolution may be understood as a low pass filter that allows lower scales (low frequency scale) only corresponding to large length scales, while filtering the higher frequency wave, i.e., the subgrid part.

A number of filters with different properties can be used. In the present study a top hat filter was used which is frequently used in combination with finite volume discretization

$$G(x-\xi, \Delta) = \begin{cases} \frac{1}{\Delta^3}, & |x-\xi| \leq \frac{\Delta}{2} \\ 0, & \text{otherwise} \end{cases} \quad (3)$$

It can be observed from Eq. (3), that the value obtained with filtering is basically averaged over a rectangular volume Δ^3 and a common choice for Δ is the cubic root of the volume of computational cell,

$$\Delta = \sqrt[3]{\Delta x \Delta y \Delta z} \quad (4)$$

where Δx , Δy and Δz denote the cell sizes along the coordinate axes. An appropriate choice of cut-off filter width Δ makes $\bar{\varnothing}$ equal to average value of \varnothing in the computational cell. This implies that explicit filtering need not be performed during the computational procedure. Instead filtering is performed along with the discretization method itself. The continuity equation after applying the filter may be written as

$$\frac{\partial \bar{u}_i}{\partial x_i} = 0 \quad (5)$$

The filtered Navier-Stokes equations may be written as

$$\frac{\partial \bar{u}_i}{\partial t} + \frac{\partial}{\partial x_j} \bar{u}_i \bar{u}_j = -\frac{\partial \bar{p}}{\partial x_i} + \nu \frac{\partial^2 \bar{u}_i}{\partial x_j \partial x_j} \quad (6)$$

Table 3 Grid sizes used in the present study

Mesh size	Re	y^+	Averaging time (t^*)
M1 16,268,000 (1660 × 140 × 70)	20,000	<1	1000 (900–1900)
M2 8,228,000 (1360 × 110 × 55)	20,000	<5	1000 (900–1900)

In Eq. (6) complications arise due to nonlinear advection terms, termed as the closure problem. Here a SGS stress tensor \mathbf{T} , and its component may be defined as

$$T_{ij} = \bar{u}_i \bar{u}_j - \bar{u}_i \bar{u}_j \quad (7)$$

If T_{ij} is inserted in Eq. (6), the following form of the filtered Navier-Stokes equations is obtained

$$\frac{\partial \bar{u}_i}{\partial t} + \frac{\partial}{\partial x_j} \bar{u}_i \bar{u}_j = -\frac{\partial \bar{p}}{\partial x_i} - \frac{\partial T_{ij}}{\partial x_j} + \nu \frac{\partial^2 \bar{u}_i}{\partial x_j \partial x_j} \quad (8)$$

In order to close the above set of equations, the tensor \mathbf{T} needs to be modelled, which is accomplished by using suitable subgrid scale (SGS) models. The four SGS models considered in the present study are presented in the following subsection.

3.1 Subgrid stress modelling

A number of SGS models have been proposed by different researchers, but a small number of models have been implemented and tested for general purpose CFD computations [28]. Most SGS models are based on the Boussinesq assumption according to which SGS stress can be modelled in a manner similar to the viscous stress [28]. Most RANS based turbulence models use an analogous idea. It can be mathematically stated as

$$\mathbf{T} = \frac{1}{3} \text{Tr}(\mathbf{T}) \mathbf{I} + \nu_{SGS} (\nabla \mathbf{u} + \nabla^T \mathbf{u}) \quad (9)$$

where \mathbf{T} denotes subgrid scale tensor, $\text{Tr}(\mathbf{T})$ its trace, \mathbf{I} the identity matrix and ν_{SGS} the SGS viscosity which is calculated from the filtered velocity field.

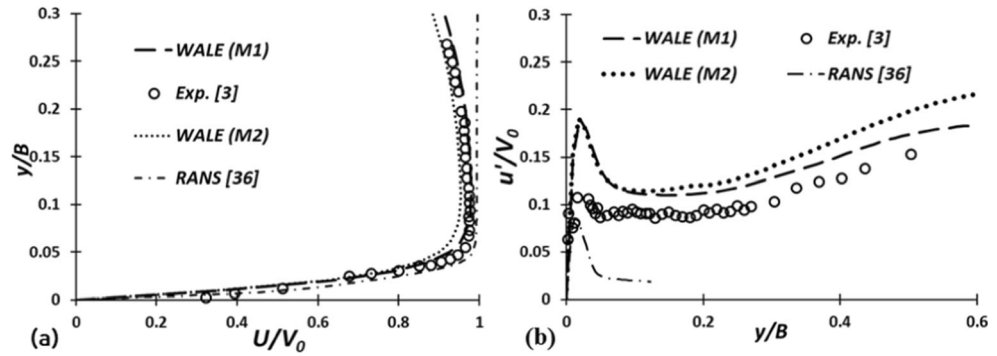
The subgrid scale kinetic energy is defined as

$$k_{SGS} = \frac{1}{2} \left(\overline{u_k^2 - \bar{u}_k^2} \right) \quad (10)$$

3.1.1 Smagorinsky model

It is a zero equation algebraic eddy-viscosity model. In this model the rotation rate is not used to calculate ν_{SGS} . This model is one of the simplest and earliest SGS models and is widely used in engineering computations. It assumes the local equilibrium to compute k_{SGS} . Here the value of the constant C_s

Fig. 3 Profiles of a normalized mean streamwise velocity and b r.m.s. fluctuations in streamwise velocity at $x/B = 3$ for $H/B = 4$ and $Re = 20,000$ using WALE model



must be defined *a priori*. This model is known to be inaccurate in laminar to turbulent transition [29]. A weakness of this model concerns the use of a single value of the constant C_s , because it should be flow dependent and must vary in time and space [30]. The form of the Smagorinsky model used in the present study is based on OpenFOAM 4.1 formulation [31].

The local equilibrium between SGS energy dissipation and production rate may be written as

$$\varepsilon_{SGS} \equiv \left(\nu \frac{\partial \overline{u_i}}{\partial x_j} \frac{\partial \overline{u_i}}{\partial x_j} - \nu \frac{\partial \overline{u_i}}{\partial x_j} \frac{\partial \overline{u_i}}{\partial x_j} \right) = -T_{ij} \overline{S}_{ij} \tag{11}$$

The eddy viscosity approximation may be written as

$$T_{ij}^a = -2\nu_{SGS} \overline{S}_{ij} \tag{12}$$

In this SGS model the eddy viscosity is assumed to be proportional to the subgrid characteristic length scale Δ and the local strain rate $|\overline{S}|$ after dimensional analysis and scaling.

$$\nu_{SGS} = (C_s \Delta)^2 |\overline{S}| \tag{13}$$

where $|\overline{S}| = \sqrt{2\overline{S}_{ij}\overline{S}_{ij}}$ and C_s denotes a model constant or Smagorinsky constant and it may be obtained [31, 32] with an assumption that the cut-off wave number (i.e., $\kappa_c = \pi/\Delta$) is present in the limit of $\kappa^{-5/3}$ Kolmogorov cascade of energy spectrum (Fig. 1b) with an approximate value as

$$C_s = \frac{1}{\pi} \left(\frac{3C_k}{2} \right)^{-3/4} \tag{14}$$

with the Kolmogorov constant $C_k = 1.4$ the value of C_s is approximately equal to 0.18.

The Smagorinsky model is implemented in OpenFOAM with the help of SGS kinetic energy. Here SGS kinetic energy is calculated by assuming a local equilibrium which provides estimates of both k and ε separate from the sub-grid scale viscosity.

$$\overline{B} = \frac{2}{3} k_{SGS} I - 2 \nu_{SGS} dev(\overline{S}) \tag{15}$$

where $\overline{S} = \frac{1}{2} \left(\frac{\partial \overline{u_i}}{\partial x_j} + \frac{\partial \overline{u_j}}{\partial x_i} \right)$ denotes the local strain rate.

The SGS kinetic energy is calculated with the help of a double dot product of two second order tensors as $\overline{S} : \overline{B} + C_e \frac{k_{SGS}^{3/2}}{\Delta} = 0$ and $\nu_{SGS} = C_k \sqrt{k_{SGS}} \Delta$.

$$\overline{S} : \left(\frac{2}{3} k_{SGS} I - 2 C_k \sqrt{k_{SGS}} \Delta dev(\overline{S}) \right) + C_e \frac{k_{SGS}^{3/2}}{\Delta} = 0 \tag{16}$$

$$\sqrt{k_{SGS}} \left\{ \frac{C_e}{\Delta} k_{SGS} + \frac{2}{3} Tr(\overline{S}) \sqrt{k_{SGS}} - 2 C_k \Delta (dev(\overline{S}) : \overline{S}) \right\} = 0 \tag{17}$$

Equation (17) may be written in the following form

$$a k_{SGS} + b \sqrt{k_{SGS}} - c = 0 \tag{18}$$

In Eq. (18) k_{SGS} is calculated as

$$k_{SGS} = \left(\frac{-b + \sqrt{b^2 + 4ac}}{2a} \right)^2 \tag{19}$$

where $a = \frac{C_e}{\Delta}$, $b = \frac{C_e}{\Delta} Tr(\overline{S})$, $c = 2 C_k \Delta (dev(\overline{S}) : \overline{S})$

For an incompressible flow, $b = \frac{2}{3} Tr(\overline{S}) = 0$, $c = 2 C_k \Delta (dev(\overline{S}) : \overline{S}) = C_k \Delta |\overline{S}|^2$. The substitution of these variables in Eq. (19) results in

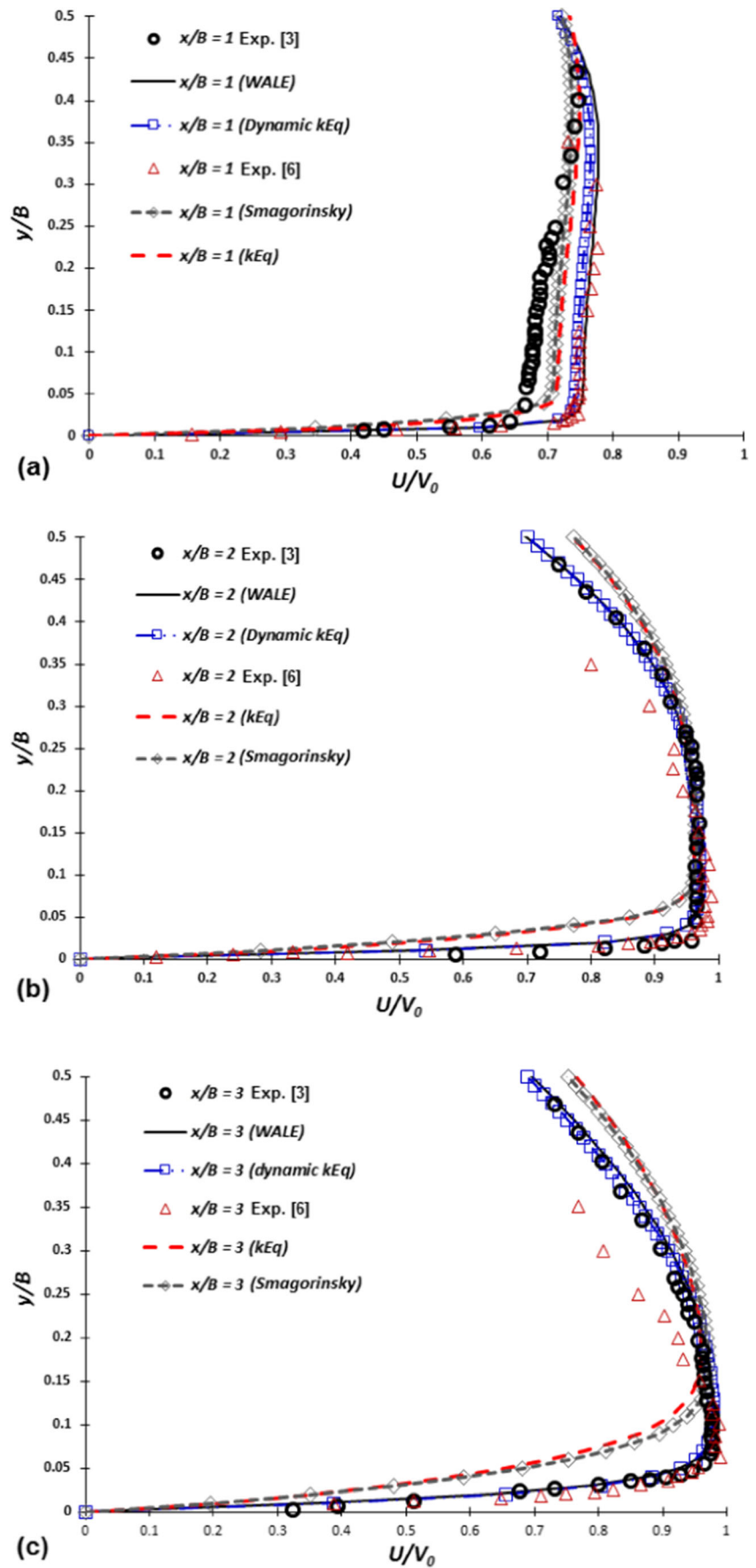
$$k_{SGS} = \frac{c}{a} = \frac{C_k \Delta |\overline{S}|^2}{C_e} \tag{20}$$

$$\nu_{SGS} = C_k \sqrt{\frac{C_k}{C_e}} \Delta^2 |\overline{S}| \tag{21}$$

By comparing Eqs. (13) and (21) for ν_{SGS} , an expression for the value of the model constant C_s may be written as

$$C_s^2 = C_k \sqrt{\frac{C_k}{C_e}} \tag{22}$$

Fig. 4 Profiles of normalized mean streamwise velocity at **a** $x/B = 1$, **b** $x/B = 2$ and **c** $x/B = 3$ for $H/B = 4$ and $Re = 20,000$ using four SGS models



where C_k and C_e denote model constants and in the present study their values were taken as 0.094 and 1.048 resulting in $C_s \approx 0.17$, nearly same as that calculated from Eq. (15). Here the effective eddy kinematic viscosity may be calculated as

$$\nu_{eff} = \nu_{SGS} + \nu \tag{23}$$

3.1.2 Wall adapting local eddy-viscosity (WALE) SGS model

The WALE model is known to perform well for flows with laminar to turbulence transition [32]. It is based on the square of the velocity gradient tensor in order to account for the influence of strain and rotation rate of the resolved turbulence fluctuations. The sub-grid scale viscosity is computed as $\nu_{SGS} = C_k \Delta \sqrt{k_{SGS}}$ where C_k denotes a model constant and k_{SGS} the subgrid scale kinetic energy.

The subgrid scale kinetic energy is obtained from the expression

$$k_{SGS} = \left(\frac{C_w^2 \Delta}{C_k}\right)^2 \frac{(S_{ij}^d S_{ij}^d)^3}{\left(\left(\overline{S_{ij} S_{ij}}\right)^{5/2} + \left(\overline{S_{ij} S_{ij}}\right)^{5/4}\right)^2} \tag{24}$$

here $\overline{S_{ij}}$ denotes the resolved strain rate tensor $\overline{S_{ij}} = \overline{\mathbf{S}} = \frac{1}{2} \left(\frac{\partial \overline{u_i}}{\partial x_j} + \frac{\partial \overline{u_j}}{\partial x_i}\right)$.

The traceless symmetric part of the square of the velocity gradient tensor [32] is calculated as

$$S_{ij}^d = \frac{1}{2} \left(\frac{\partial \overline{u_k}}{\partial x_i} \frac{\partial \overline{u_j}}{\partial x_k} + \frac{\partial \overline{u_k}}{\partial x_j} \frac{\partial \overline{u_i}}{\partial x_k}\right) - \frac{1}{3} \delta_{ij} \frac{\partial \overline{u_k}}{\partial x_l} \frac{\partial \overline{u_l}}{\partial x_k} \tag{25}$$

here δ_{ij} denotes the Kronecker delta.

The final expression for ν_{SGS} by substituting the expression for k_{SGS} in $\nu_{SGS} = C_k \Delta \sqrt{k_{SGS}}$ may be written as

$$\nu_{SGS} = (C_w \Delta)^2 \frac{(S_{ij}^d S_{ij}^d)^{3/2}}{\left(\overline{S_{ij} S_{ij}}\right)^{5/2} + \left(\overline{S_{ij} S_{ij}}\right)^{5/4}} \tag{26}$$

where C_w is a model constant, which depends on the Smagorinsky constant C_s . It was obtained by [32] for an isotropic turbulent flow field with various resolutions as $C_w^2 \approx 10.6 C_s^2$ and a value in the range of $0.55 \leq C_w \leq 0.60$ for $C_s = 0.18$ and $0.32 \leq C_w \leq 0.34$ if $C_s = 1$.

3.1.3 SGS kinetic energy (k) equation model

Another category of SGS models are the one-equation eddy-viscosity models. These models are different from the Smagorinsky model in computation of k_{SGS} , where instead

of the assumption of the local equilibrium (i.e., $P_{k_{SGS}} - \varepsilon_{k_{SGS}} = 0$) a transport equation for k_{SGS} is solved to obtain k_{SGS} [33]. Therefore the usual selection for the scale of the characteristic velocity in such models is $u_{SGS} = \sqrt{k_{SGS}}$. The one equation eddy-viscosity models are known to overcome the deficiency of the local stability assumption between the SGS energy production and dissipation used in the algebraic eddy-viscosity models. In a one equation SGS model a transport equation for resolved turbulence kinetic energy (k_{SGS}) is solved to consider the effects of history due to production, dissipation and diffusion that have the capability to improve their performance when applied to complex flow situations with non-equilibrium turbulence [34]. Similar to Smagorinsky SGS model, the one-equation eddy-viscosity model uses the approximation of eddy-viscosity.

Transport equation of k_{SGS}

$$\frac{\partial k_{SGS}}{\partial t} + \frac{\partial \overline{u_i} k_{SGS}}{\partial x_i} = 2\nu_{SGS} |\overline{D_{ij}}|^2 - C_e \frac{k_{SGS}^{3/2}}{\Delta} + \frac{\partial}{\partial x_i} \left(\nu_{SGS} \frac{\partial k_{SGS}}{\partial x_i} \right) + \nu \frac{\partial^2 k_{SGS}}{\partial x_i \partial x_i} \tag{27}$$

The SGS kinematic viscosity (ν_{SGS}) may be defined as $\nu_{SGS} = C_k \Delta \sqrt{k_{SGS}}$ here the default model constants are $C_e = 1.048$ and $C_k = 0.094$. $\overline{D_{ij}}$ denotes the filtered strain rate. It can be observed that four independent terms appear on the R.H.S. of Eq. (27), which may be termed as (i) the production of turbulence by resolved scales, (ii) turbulent dissipation, (iii) turbulent diffusion and (iv) viscous dissipation. Here $k_{SGS} = Tr(B)/2$ and hence this expression may be used to calculate the isotropic sub-grid stress.

3.1.4 Dynamic SGS turbulence kinetic energy (k) equation model

In the algebraic models the subgrid scale stresses are parameterized by the resolved velocity scales with the assumption of the local equilibrium of transferred energy through grid filter scale and dissipation of turbulence kinetic energy at small subgrid scales. A dynamic SGS kinetic energy model is a one-equation subgrid model in which the subgrid scale turbulence calculation can be improved by solving a transport equation for subgrid scale turbulence kinetic energy in which the model constants are evaluated by a dynamic procedure [35]. The formulation of Kim and Menon [35] is used in the present study. The subgrid scale kinematic eddy viscosity may be computed using k_{SGS} as $\nu_{SGS} = C_k \sqrt{k_{SGS}} \Delta$.

Further the subgrid scale stress may be written as

$$T_{ij} - \frac{2}{3} k_{SGS} \delta_{ij} = -2C_k \sqrt{k_{SGS}} \Delta \overline{S_{ij}} \tag{28}$$

Fig. 5 Profiles of normalized mean streamwise velocity at **a** $x/B = 4$, **b** $x/B = 5$ and **c** $x/B = 6$ for $H/B = 4$ and $Re = 20,000$ using four SGS models

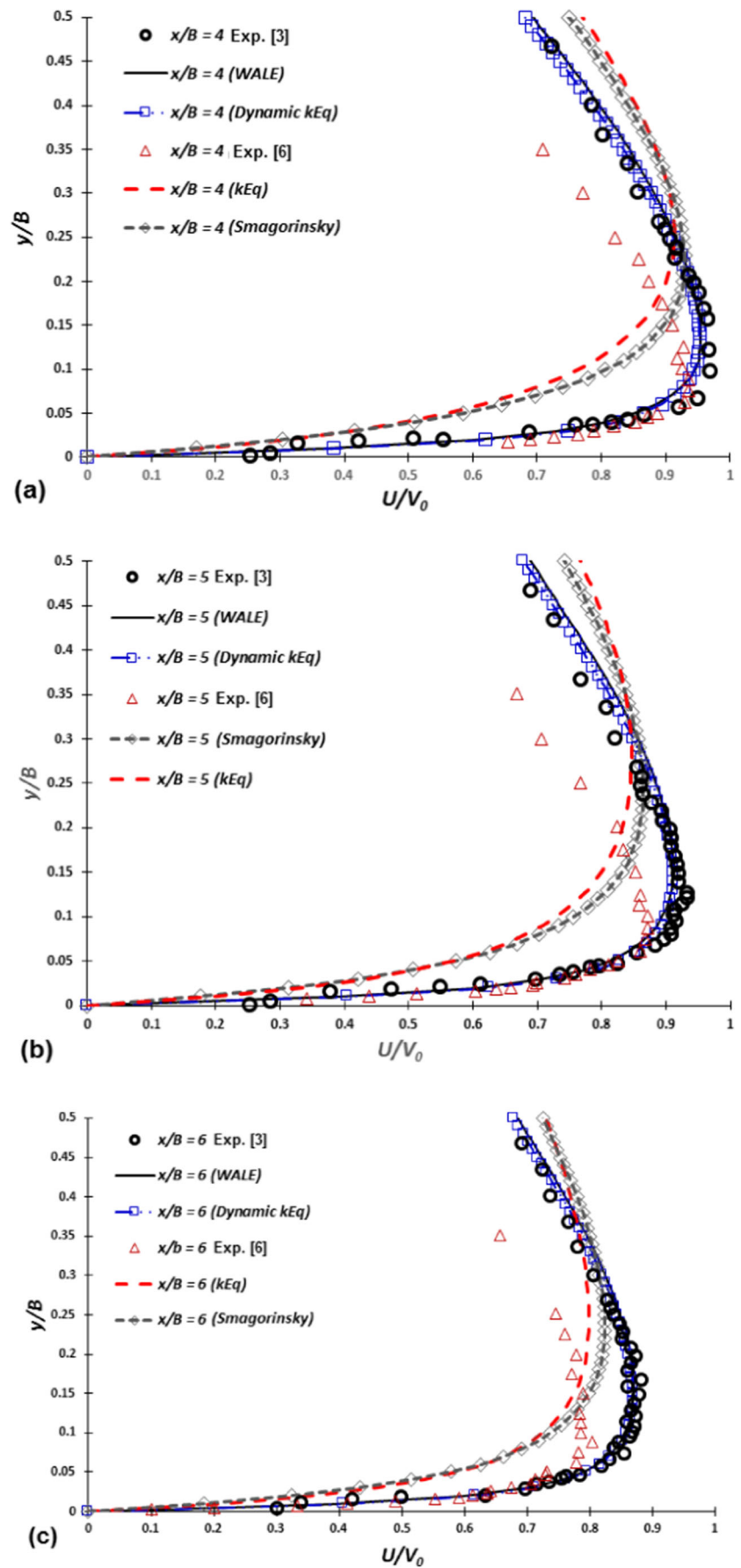
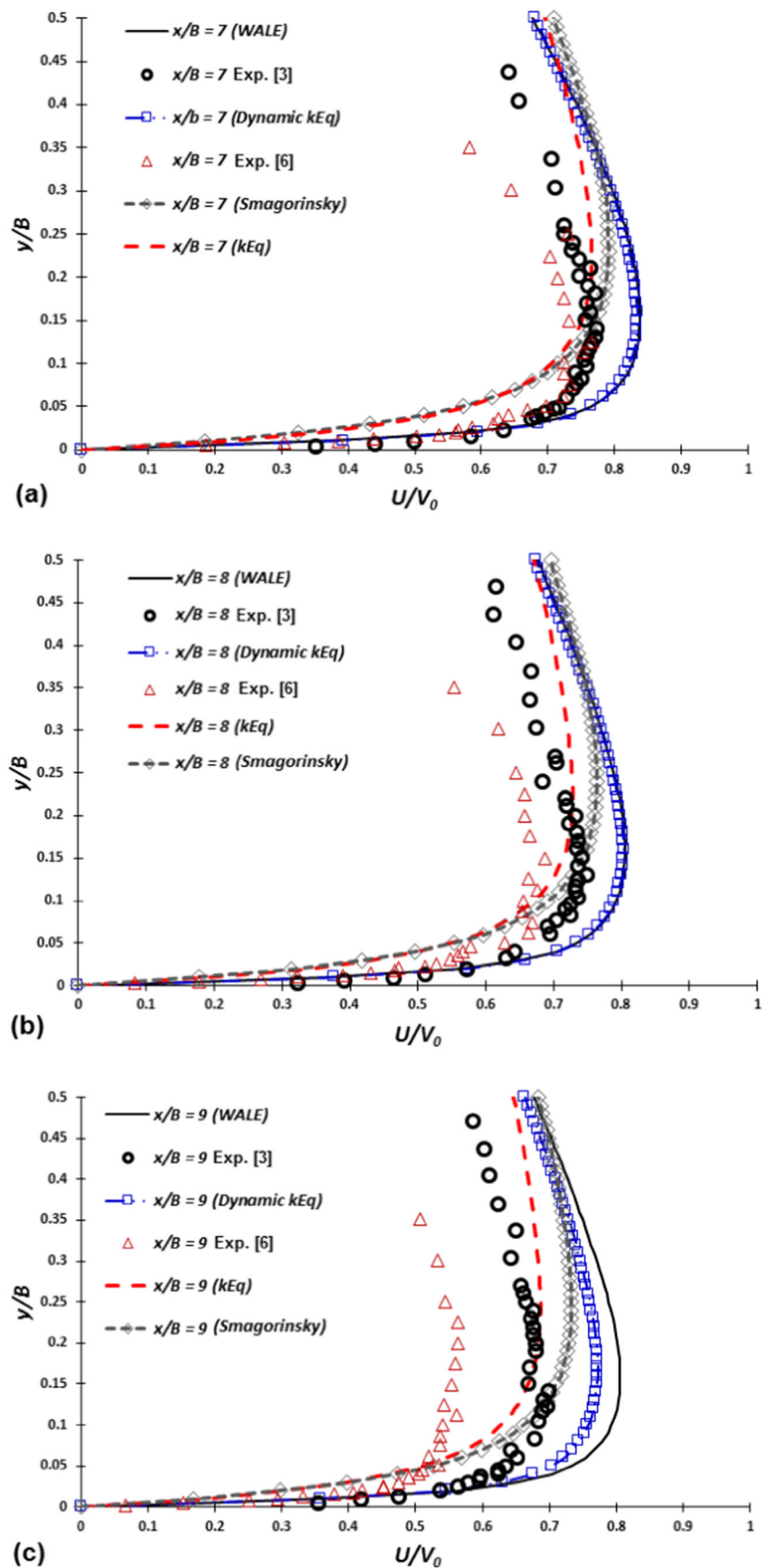


Fig. 6 Profiles of normalized mean streamwise velocity at a $x/B = 7$, **b** $x/B = 8$ and **c** $x/B = 9$ for $H/B = 4$ and $Re = 20,000$ using four SGS models



here k_{SGS} is obtained by solving the following transport equation

$$\frac{\partial \bar{k}_{SGS}}{\partial t} + \frac{\partial \bar{u}_i \bar{k}_{SGS}}{\partial x_i} = -T_{ij} \frac{\partial \bar{u}_i}{\partial x_j} - C_e \frac{\sqrt{k_{SGS}^3}}{\Delta} + \frac{\partial}{\partial x_i} \left(\nu_{SGS} \frac{\partial k_{SGS}}{\partial x_i} \right) \quad (29)$$

where C_k and C_e denote the model constants and these may be determined dynamically [35], i.e., from the local flow properties and the value of σ_k may be taken as unity. R.H.S of Eq. (29), contains three independent terms, namely, production, rate of dissipation and transport rate of SGS turbulence kinetic energy, respectively.

The subgrid scale kinematic eddy-viscosity ν_{SGS} does not show correct behaviour in the limit of $y \rightarrow 0$ (here y denotes the distance from the wall). A damping function is employed to correct this behavior, i.e., the van Driest damping function, given as

$$f = \frac{k}{C_\Delta} \left(1 - e^{-y^+/A^+} \right) \quad (30)$$

where $k = 0.41$ denotes the von Karman constant, $C_\Delta = 0.158$ and $A^+ = 26$.

For incompressible flows the instantaneous energy equation may be written as

$$\frac{\partial e}{\partial t} (\rho e) + \frac{\partial}{\partial x_j} (\rho e u_j) = -\frac{\partial q_k}{\partial x_k} \quad (31)$$

where e denotes the internal energy and q_k the conductive heat flux. If filtering operation is applied to Eq. (31) the following filtered energy equation is obtained

$$\frac{\partial e}{\partial t} (\rho \bar{e}) + \frac{\partial}{\partial x_j} (\rho \bar{e} u_j) = -\frac{\partial q_{tk}}{\partial x_k} - \frac{\partial \bar{q}_k}{\partial x_k} \quad (32)$$

here $q_{tk} = \left(\overline{\rho e u'_k} + \overline{\rho e' u_k} + \overline{\rho e' u'_k} \right)$ denotes the turbulent heat flux. According to the Fourier's law of heat conduction $\bar{q}_k = -k \frac{\partial \bar{T}}{\partial x_k}$, here k denotes the thermal conductivity. Similarly, turbulent heat flux may be written by using the analogy as $q_{tk} = -k_t \frac{\partial \bar{T}}{\partial x_k}$. With $e = C_p T$, Eq. (32) may be written for the resolved temperature for a constant density with $Pr = C_p \mu_0 / k$ and $Pr_t = C_p \mu_t / k_t$ as

$$\frac{\partial \bar{T}}{\partial t} + \frac{\partial}{\partial x_j} (\bar{T} u_j) = \frac{\partial}{\partial x_k} \left[\left(\frac{\nu_t}{Pr_t} + \frac{\nu_0}{Pr} \right) \frac{\partial \bar{T}}{\partial x_k} \right] \quad (33)$$

where $k_{eff} = \frac{\nu_t}{Pr_t} + \frac{\nu_0}{Pr}$. Finally the resolved temperature equation becomes

$$\frac{\partial \bar{T}}{\partial t} + \frac{\partial}{\partial x_j} (\bar{T} u_j) = \frac{\partial}{\partial x_k} \left(k_{eff} \frac{\partial \bar{T}}{\partial x_k} \right) \quad (34)$$

Some parameters used in the present study are defined as, Reynolds number $Re = \frac{uB}{\nu}$ and Nusselt number $Nu = \frac{hB}{k}$, here B denotes the slot width and h the heat transfer coefficient calculated as $h = \frac{\dot{q}_w}{(T_w - T_0)} = -\frac{\dot{q}_w}{(T_w - T_0)} \left(\frac{\partial T}{\partial y} \right)_{y=0}$. By substituting h (in terms of the temperature gradient at $y = 0$) in the expression for Nu results in the following expression

$$Nu = \frac{hB}{k} = -\frac{B}{(T_w - T_0)} \left(\frac{\partial T}{\partial y} \right)_{y=0} \quad (35)$$

4 Computational strategy

OpenFOAM 4.1 was used for computations in the present study. It is an open source CFD software based on C++ programming language. It is based on FVM (finite-volume method) using co-located methodology and a variety of interpolation, discretization and matrix solution schemes can be selected from *fvSchemes* and *fvSolution* dictionary in the system folder. OpenFOAM solver comprises of basic CFD solver, RANS and LES computation capabilities for incompressible and compressible flows with heat transfer, DNS and particle tracking, etc. It also provides tools to perform parallel processing or computation by decomposition of geometry and its reconstruction. In addition to these standard solvers, its code can be modified for new customized solvers or boundary conditions, etc., according to requirements. Thus OpenFOAM can be seen as a generic, programmable tool to solve a variety of complex CFD problems. In OpenFOAM the dictionary *turbulenceProperties* contains *simulationType* keyword which is read by solver, where one may provide details of turbulence modelling techniques to be used, such as, laminar (for no modelling), RAS (for RANS modelling) and LES, etc. If LES is selected, it requires additional information, such as, name of SGS model, coefficients for the selected model, etc.

A second-order implicit scheme was considered for the discretization of the time dependent terms in the governing eqs. A non-dimensional time step, $\Delta t^* = \Delta t V_0 / B$, of the order of 1×10^{-3} and a dynamic adjustable Courant (CFL) number less than unity were used. A non-dimensional time unit (t^*) was defined ($t^* = t V_0 / B$) to monitor the computations. All cases were monitored for the steady behavior. A volume-averaged resolved kinetic energy was observed and nearly 900 non-dimensional time units (t^*) were

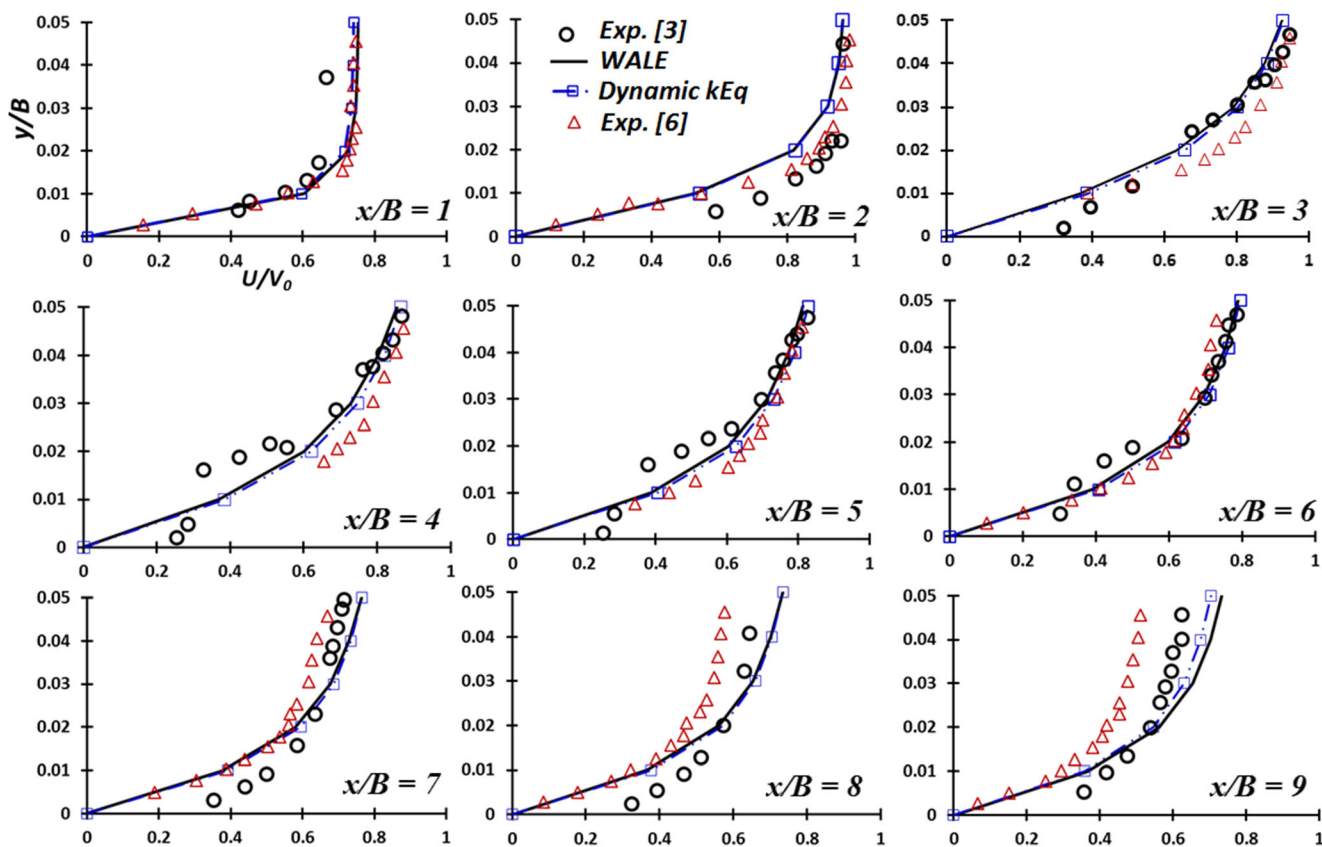


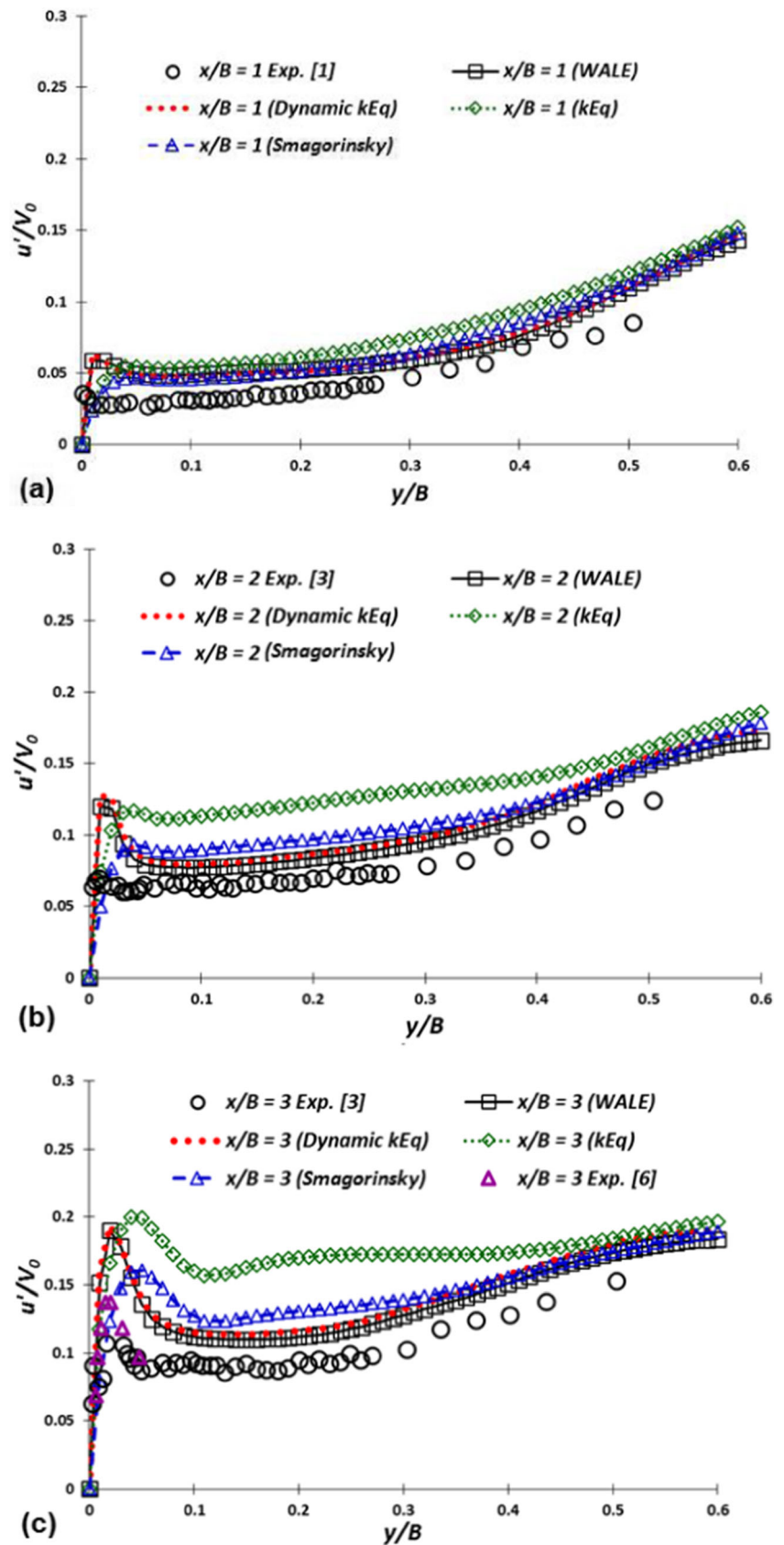
Fig. 7 Profiles of normalized streamwise velocity at $1 \leq x/B \leq 9$ quite close to impingement plate ($y/B=0-0.05$) for $H/B=4$ and $Re=20,000$ using WALE and dynamic k -equation models

required to reach the steady behavior. All the data presented, such as, velocity, Reynolds stresses, etc., were time-averaged with nearly 1000 non-dimensional time units and spatially-averaged in the spanwise direction as well. The *buoyantBoussinesqPimpleFoam*, a FVM based transient solver, was used. It uses the PIMPLE algorithm for the pressure-velocity coupling, a combination of PISO (pressure implicit with splitting operators) and SIMPLE (semi-implicit method for pressure linked equation) algorithms with a collocated grid arrangement. For the computation of flux in the convection terms the central-differencing scheme was used for the discretization. The diffusive terms of the equations were also discretized using the central differencing scheme. We have used *smoothSolver* with *symGaussSeidel* smoother to solve the linear system of equations for the conservation of momentum, energy and turbulence. However GAMG (geometric agglomerated algebraic multi grid) solver was used for the linear system of equations for pressure. Solutions were assumed to be converged when residuals of all the equations were of the order of 1×10^{-6} . Table 2 shows different properties of air used in the present study. The effects of compressibility and temperature-dependence on properties of air were neglected in the present study.

5 Results and discussion

Four SGS closure models, namely, Smagorinsky, WALE, one-equation SGS turbulence kinetic energy (k) and dynamic SGS turbulence kinetic energy (k) equation, were considered for large eddy simulation (LES) of jet impingement on a heated surface at a low nozzle to plate spacing ($H/B=4$) with $Re=20,000$. Normalized coordinates were used to present various results, such as, normalized streamwise direction (x/B), normalized wall normal direction (y/B), normalized velocities or turbulence kinetic energy (U/V_0 , u'/V_0 or k/V_0^2) and normalized Nusselt number (Nu/Nu_{st}), etc. In the present configuration $x/B=0$ represents the jet centerline and $x/B=0$, $y/B=0$ the stagnation point from where a wall jet region develops on either side of the jet centerline (Fig. 2). The region affected by the stagnation ranges from $x/B=0$ to 3 [3]. Assessment of four SGS models in the present study is based on a comparison of the computed results with the experimental data of Ashforth-Frost et al. [3] and Zhe and Modi [6]. Nine locations were considered in the streamwise direction covering the stagnation zone as well as the development of wall jet region resulting in complex flow behaviours. Computations of such regions is a challenging task. The profiles of the streamwise velocity and

Fig. 8 Profiles of normalized r.m.s. fluctuations in streamwise velocity at **a** $x/B=1$, **b** $x/B=2$ and **c** $x/B=3$ for $H/B=4$ and $Re=20,000$ using four SGS models



r.m.s. fluctuations of streamwise velocity at all these locations with four SGS models were investigated. Profiles of normalized Nusselt numbers have also been compared with the experimental data [3]. Further contours of various flow features, such as, instantaneous velocity, mean velocity, turbulence kinetic energy and normalized Q criterion have also been presented and analyzed.

All the simulations consisted of two stages. In the first stage sampling of statistics were not performed (first $t^* = 900$) because all unsteady simulations had to pass through initial conditions and flow development process. In the second stage, also called the averaging phase, time-averaging was performed for a time (t^* from 900 to 1900) much more than a characteristic flow time scale in order to reduce statistical errors. Further two meshes $M1$ and $M2$ (Table 3) were used to assess the effect of coarse and fine grids on the present LES results. The most important task in a LES simulation is a selection of an optimum grid that falls in the range of the inertial sub-range because grid is implicitly used in the filtering operation.

Figure 3 shows comparisons of the streamwise velocity profiles using different grids ($M1$ and $M2$) for the WALE model with the experimental data [3]. The profiles of the streamwise velocity and r.m.s. velocity fluctuations with the fine grid ($M1$) are more accurate than the ones using the coarse grid ($M2$) (Fig. 3). This behavior is expected in LES simulations because mesh refinement results in a finer filter for which the energy spectrum will shift towards high values of κ (Fig. 1b). Hereafter fine grid ($M1$) was used in all the subsequent simulations. Figure 3a, b also shows a comparison of the present LES results with the predictions by RANS based SST $k-\omega$ turbulence model [36]. It can be observed that the SST $k-\omega$ turbulence model [36] overpredicts the mean streamwise velocity and underpredicts the r.m.s. streamwise velocity compared to the experimental results [3]. On the other hand the LES results of mean and r.m.s. velocities by the WALE model match quite well with the experimental data [3]. Further the quality of the present LES grid was assessed by a criterion called $LES_IQ_v = 1/[1 + \{0.05(\langle v + \nu_{SGS} \rangle / \nu)^{0.53}\}]$ [8] originally proposed by Celik et al. [37], who suggested that the index of quality (LES_IQ_v) should be larger than 0.8 for a well resolved LES grid. The value of the LES_IQ_v were observed to be in the range of 0.80–0.95 for the present LES grid ($M1$) considered for computations.

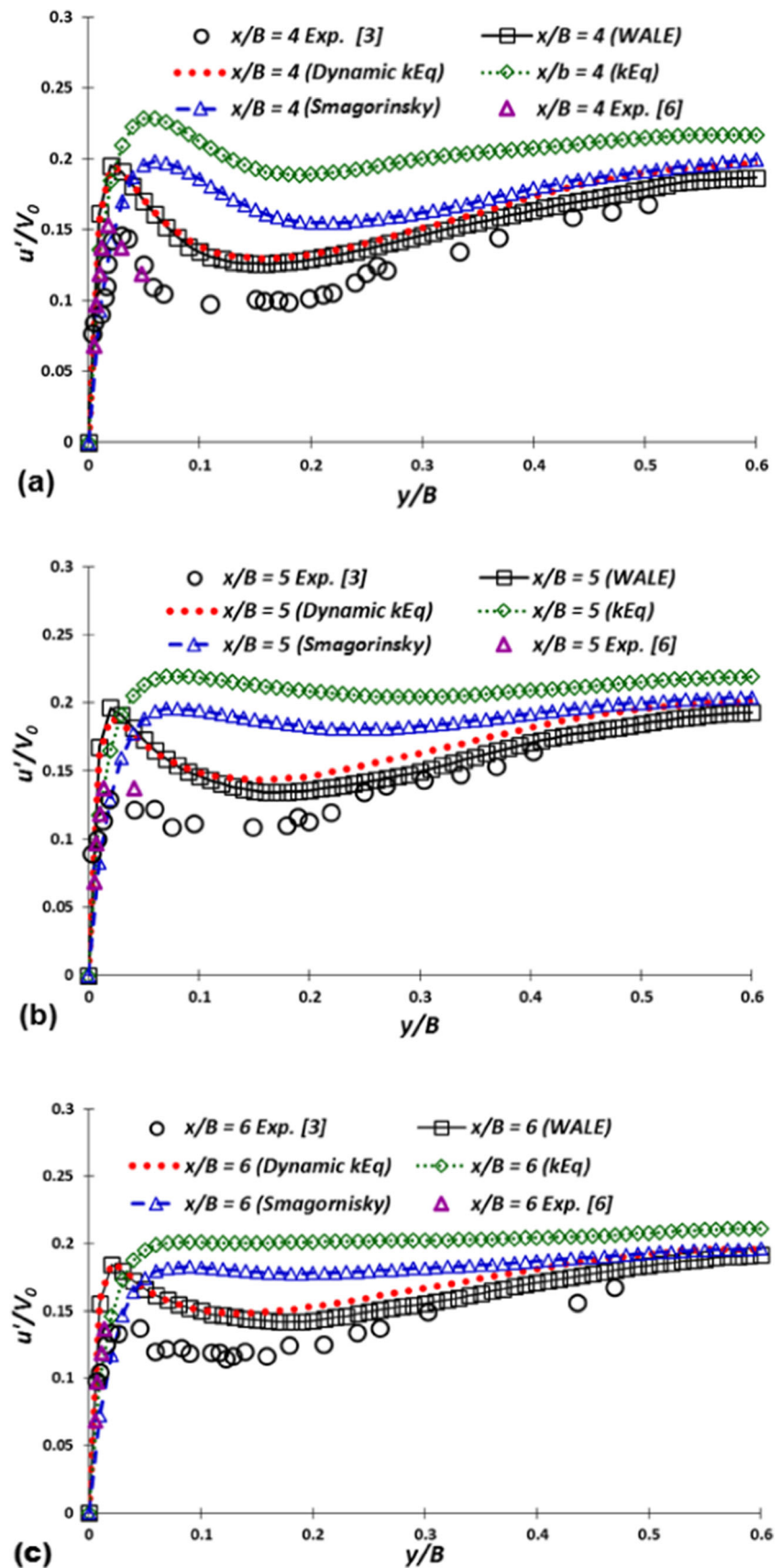
Figure 4 shows the profiles of the normalized mean streamwise velocity close to the impingement plate ($y/B = 0-0.5$) at (a) $x/B = 1$, (b) $x/B = 2$ and (c) $x/B = 3$. These streamwise locations cover the region affected by stagnation, thus physically it is a complex flow region. At $x/B = 1$ (close to the stagnation point) the profiles of the normalized streamwise velocity predicted by WALE and

dynamic k -equation SGS models match quite well up to $y/B = 0.05$, i.e., in the vicinity of the wall (Fig. 4a) with the experimental data [3, 6]. The LES data presented have been averaged in time and space (in the spanwise z -direction). However, it can be observed from Fig. 4a that for $y/B \geq 0.05$ the normalized mean streamwise velocity computed using WALE and dynamic k -equation models shows some deviations with the experimental data [3], but a good agreement can be observed with the other experimental data [6] along the wall normal direction (i.e., along y/B). The deviations observed are smaller using Smagorinsky and k -equation SGS models. However, these models show some deviations quite close to the wall. It can be observed that all the SGS models predict the same trend as in the experimental data [3, 6].

Flow behavior of the present configuration at $x/B = 1$ is considered to be quite complex and thus computation of this region is a challenging task. It can be observed that all the SGS models perform well in this region with a maximum 11% deviation from the experimental data [3] between $y/B = 0.05-0.35$ (Fig. 4a). One can observe a sharp increase in the streamwise velocity with y/B (up to $y/B = 0.05$) near the impingement plate for $x/B = 1, 2$ and 3 [Figs. 4(a), 4(b) and 4(c)]. However at $x/B = 1$ increment in the streamwise velocity continues for $y/B \geq 0.05$ and it may be attributed to the contribution of y -velocity component. An increase in the streamwise velocity can also be observed at $x/B = 2$ similar to $x/B = 1$ but only up to $y/B = 0.25$. Thereafter it decreases due to interaction of the normal (y) velocity component. Conversely at $x/B = 3$ it decreases at higher y/B values (for $y/B \geq 0.08$). This reduction in velocity for $y/B \geq 0.08$ is because in this region the vertical component of velocity is more effective than its streamwise component. At $x/B = 2$ and 3 the maximum streamwise velocity U/V_0 in the range of 0.97–0.98 can be observed at $y/B \approx 0.08-0.1$ using WALE and dynamic k -equation models [Figs. 4(b, c)], which is similar to the experimental observations [3, 6]. The other two SGS models considered, i.e., Smagorinsky and k -equation, correctly predict the maximum value of U/V_0 but at higher y/B location compared to the experimental results (Fig. 4b, c). The profiles of the normalized mean velocity are correctly predicted using WALE and dynamic k -equation models (Fig. 4b and c). A good match can be observed with the experimental data [3, 6] with WALE and dynamic k -equation SGS models whereas computations using other two models (Smagorinsky and k -equation) show some deviations. The computed profiles of mean velocity by all the SGS model follow similar trend as in the experimental data [3, 6] for $x/B = 1, 2$ and 3.

LES is known for its capability to resolve important transient flow structures. In the present flow configuration the

Fig. 9 Profiles of normalized r.m.s. fluctuations of streamwise velocity at **a** $x/B=4$, **b** $x/B=5$ and **c** $x/B=6$ for $H/B=4$ and $Re=20,000$ using four SGS models



SGS model coefficients should be dependent on flow regime. Therefore, there is an obvious need for dynamic SGS models because the computed results using a single calibration cannot be expected to perform well universally. The present results substantiate this behavior that a dynamic formulation of SGS turbulence kinetic energy performs well compared to k -equation and Smagorinsky models. The WALE model showed improvement over the Smagorinsky model with good predictions of wall shear stress as well as turbulent quantities [38]. Nicoud and Ducros [32] observed that the WALE model performed well for flows with transition to turbulence and for near wall statistics. They found it promising for complex flow situations and also observed a proper asymptotic behaviour of the eddy viscosity using the WALE model for the case of a solid wall. They suggested that it needs to be tested for more complex cases. Further advantages of the WALE model can be seen in [32].

One of the main reasons for poor prediction by Smagorinsky and SGS kinetic energy models is the use of a constant value of the model coefficients which needs to be specified *a priori*. However in actual practice the model coefficients are not constant but are flow dependent and thus it should vary in time and space. This could be a reason for the deviation in the results using these two models in the present study with the presence of complex stagnation and wall jet development regions. On the other hand, the dynamic SGS k -equation model performs well because here the modelling coefficients do not use constant values but these are calculated dynamically during the computations. However a dynamic model may also have some drawbacks, i.e., its numerical instability can be related to large variation and negative values of the model coefficient [30]. Sohankar et al. [30] observed negative values of the local dynamic coefficient (C_k) and due to this behavior the production term of turbulence kinetic energy equation became negative and as a result occurrence of backscattering was observed.

Figure 5 shows the normalized streamwise velocity profiles near the impingement plate at (a) $x/B = 4$, (b) $x/B = 5$ and (c) $x/B = 6$. These streamwise locations are located outside the stagnation effected region. The development of wall jets can be clearly observed at these locations. The streamwise velocity decreases in magnitude downstream with spread of the wall jet (Fig. 5). The profiles of streamwise velocity (at $x/B = 4, 5$ and 6) by WALE and dynamic k -equation SGS models match quite well with the experimental data [3] and other two models, i.e., Smagorinsky and k -equation, show some deviations though all the models follow the experimental trend [3, 6]. It can also be observed that the predictions of the streamwise velocity profiles with WALE and dynamic k -equation models at $x/B = 4, 5$ and 6 show the same behavior as in experimental results of Zhe and Modi [6] with a close prediction in the vicinity of wall and some deviation at higher values of y/B (Fig. 5). This deviation is due to the fact that the

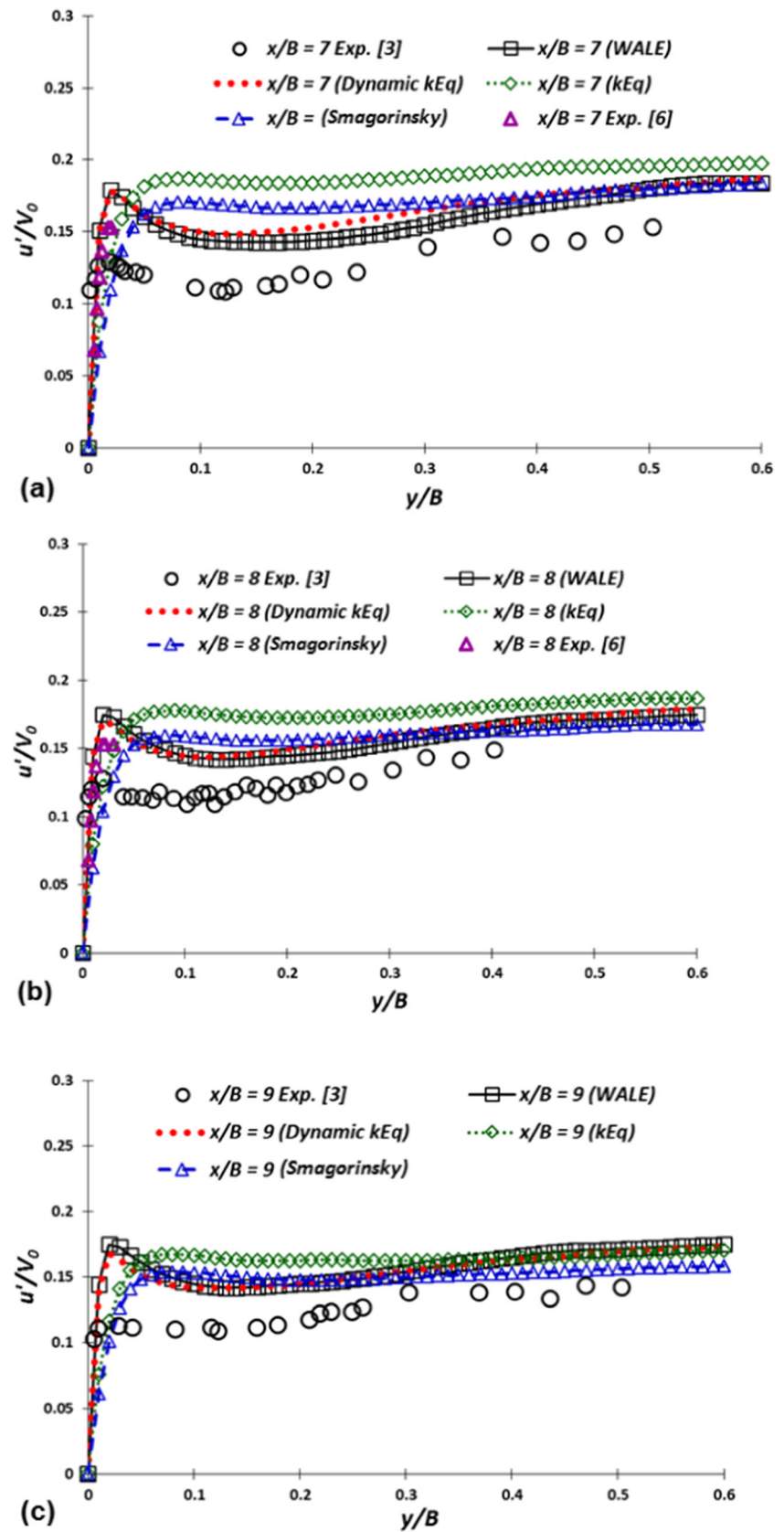
present computational setup was made in accordance with that of Ashforth-Frost et al. [3], but the values of H/B and Re were the same (4 and 20,000) in both the experimental setups. At $x/B = 2-6$ the predictions of velocity profiles match quite well with the experimental data [3] compared to that at other x/B locations. It can be concluded that the present LES computations using WALE and dynamic k -equation models are capable of providing accurate results in the region between $2 \leq x/B \leq 6$.

Figure 6 shows the streamwise velocity distributions at (a) $x/B = 7$, (b) $x/B = 8$ and (c) $x/B = 9$ along y/B . The magnitude of the maximum streamwise velocity is shifted to higher y/B values compared to that at lower x/B locations ($x/B = 1-6$). It can be observed that the computations of the velocity profile at $x/B = 7, 8$ and 9 (Fig. 6) follow the same trends as in both the experimental results [3, 6]. It can be observed that the LES models show deviations from the experimental data (Fig. 6) and downstream (from $x/B = 7-9$) the deviation increases with the maximum deviation at $x/B = 9$. WALE and dynamic k -equation models also show deviations at these x/B locations. At $x/B = 9$, where the deviation is the maximum, the WALE model shows approximately 16% and dynamic k -eq. 11% deviations compared to the experimental data [3] in the prediction of the local streamwise velocity. The SGS models show good trends at these x/B locations as that at the previous locations. From Figs. 4, 5 and 6 one can clearly observe a development of wall jet and the LES computations accurately predict this behavior. Figure 7 shows the streamwise velocity profiles quite close to the impingement plate using WALE and dynamic k -equation SGS models. The present LES computations match quite well with the experimental results [3, 6] (Fig. 7).

Figures 8, 9 and 10 show comparisons of the profiles of normalized r.m.s. velocity, u' (non-dimensional turbulence) near the impingement wall at streamwise locations between $x/B = 1-9$. The results obtained using the four SGS models were compared with the experimental data [3, 6]. The streamwise locations $x/B = 1-3$ are in the stagnation zone. It can be observed from Fig. 8a that profiles of the r.m.s. fluctuations in the streamwise velocity are in good agreement with the experimental data [3] with approximately 8% deviation. Nearly all the SGS models show good agreement and follow the trend of experimental data [3].

The profiles of the normalized r.m.s. fluctuations in the streamwise velocity at $x/B = 2$ are also in good agreement with the experimental data (Fig. 8b). The profiles of r.m.s. fluctuations by three SGS models (Smagorinsky, dynamic k -equation and WALE) are in good agreement with the experimental data [3]. However, the k -equation model shows some deviation (Fig. 8b). The deviation with k -equation model is large close to the impingement plate and it decreases with y/B , though it follows the experimental profile [3]. The predictions using WALE and dynamic k -equation models at $x/B = 3$ (Fig. 8c) agree well with the experimental data [3, 6]. The other two

Fig. 10 Profiles of normalized r.m.s. fluctuations in streamwise velocity at **a** $x/B=7$, **b** $x/B=8$ and **c** $x/B=9$ for $H/B=4$ and $Re=20,000$ using four SGS models



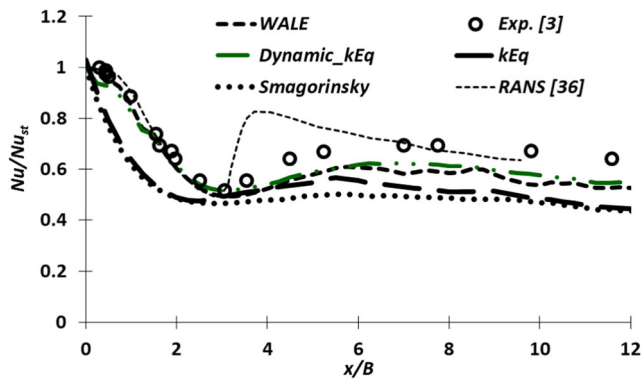


Fig. 11 Profiles of normalized local Nusselt number on impingement plate for $H/B = 4$ and $Re = 20,000$ using four SGS models

models (k -equation and Smagorinsky) again show some deviations which are large close to the wall and these decrease with y/B . The fluctuations increase gradually with y/B at $x/B = 1$ and 2. However at $x/B = 3$ the r.m.s. velocity fluctuations show two peaks (one near the wall at $y/B = 0.017$ and immediately after this point it decreases slightly and then a gradual increment in r.m.s. fluctuations can be observed at higher y/B values). WALE and dynamic k -equation SGS models show good agreement with both the experimental results [3, 6] and replicate the associated flow phenomenon at $x/B = 3$, i.e., two peaks in the r.m.s. velocity fluctuations (Fig. 8c).

Figure 9 shows the r.m.s. streamwise velocity profiles at (a) $x/B = 4$, (b) $x/B = 5$ and (c) $x/B = 6$ in the regions close to the impingement plate. Once again it can be observed that the r.m.s. streamwise velocity computed using WALE and dynamic k -equation SGS models are in good agreement with both the experimental data [3, 6]. The computations using

k -equation and Smagorinsky models show larger deviations at $x/B = 4$ and 5. However, WALE and dynamic k -equation SGS models provide a good accuracy (Fig. 9a, b). Furthermore k -equation and Smagorinsky models show smaller deviations at $x/B = 6$ (Fig. 9c) compared to that $x/B = 4$ and 5 (Fig. 9a, b). It can also be observed that of the four SGS models, the deviation using the k -equation model is large in computation of turbulence data. Two clear peaks in r.m.s. velocity can also be observed in Fig. 9a, b at $x/B = 4$ and 5. All the four SGS models considered reproduce the experimental behaviour (Fig. 9), but the computations using WALE and dynamic k -equation models were again observed to be in good agreement with the experimental results [3, 6].

Figure 10 shows the r.m.s. x -velocity profiles at (a) $x/B = 7$, (b) $x/B = 8$ and (c) $x/B = 9$ (the outer wall jet regions). The r.m.s. velocity fluctuations computed using WALE and dynamic k -equation models are in good agreement with the experimental results [3, 6]. At these x/B locations the Smagorinsky model also performs well. Here as well the k -equation model overpredicts the turbulence profiles compared to that by other three models. It can be concluded that the values of r.m.s. velocity fluctuations increase rapidly with the normal distance from the impingement plate. All the SGS models follow the behavior of the experimental results [3, 6]. Among the four SGS models, WALE and dynamic k -equation models perform better than other two SGS models (Figs. 8–10).

Figure 11 shows profiles of the time-averaged local Nusselt number normalized with the corresponding stagnation point Nusselt numbers on the impingement plate ($H/B = 4$ and $Re = 20,000$). The four SGS models show a secondary peak in Nu , similar to that in the experimental data [3]. The local Nu profiles computed using WALE and dynamic k -equation SGS

Fig. 12 Contours of **a** instantaneous velocity and **b** x -velocity magnitude for $H/B = 4$ and $Re = 20,000$ using dynamic k -equation model ($t^* = 1900$)

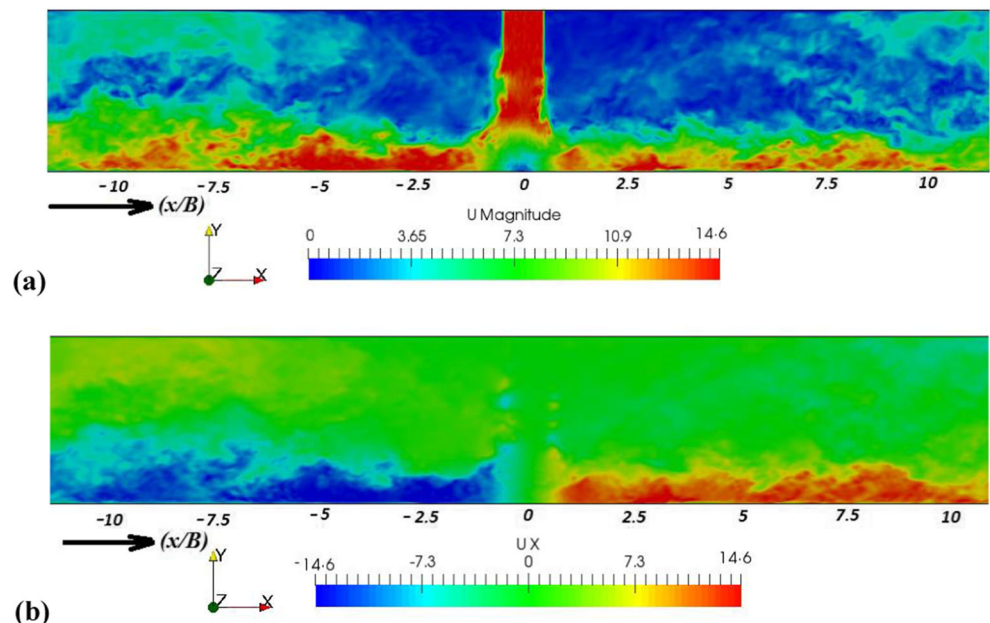
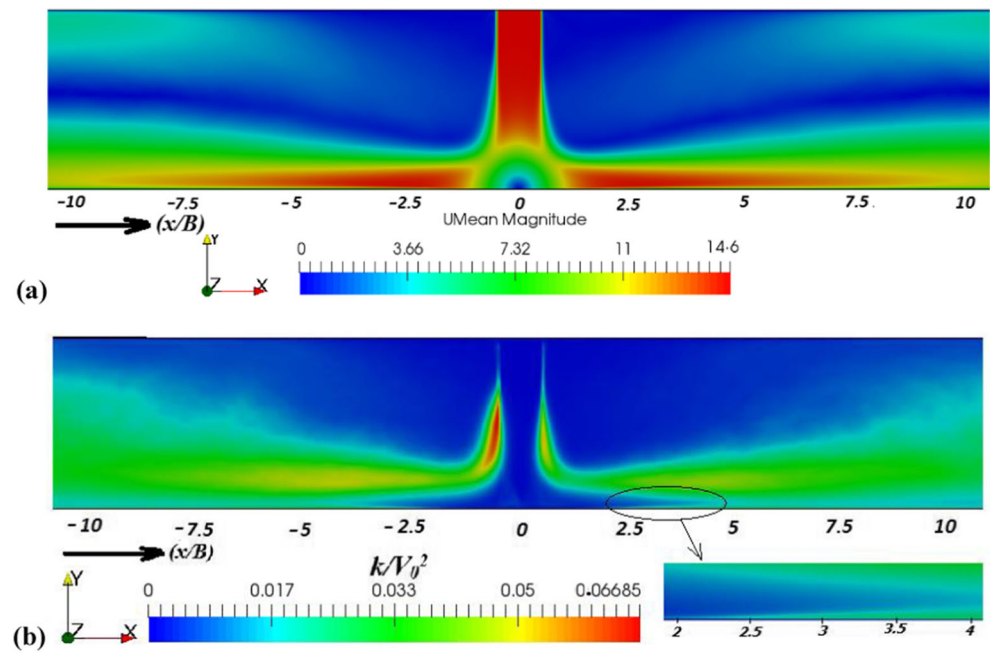


Fig. 13 Contours of **a** time-averaged mean velocity and **b** turbulence kinetic energy for $H/B = 4$ and $Re = 20,000$ using dynamic k -equation model ($t^* = 1900$)



models are in close agreement with the experimental data [3], which shows a dip approximately at $x/B = 3$ (Fig. 11). WALE and dynamic k -equation models also show a dip in Nu profile at the same location and the computations are in good agreement with [3] for $x/B \leq 3$. For $x/B \geq 3$ Nu increases gradually and a secondary peak in its distribution can be observed (Fig. 11). The Nusselt number profiles using WALE and dynamic k -equation models for $x/B > 3$ show a good agreement with approximately 11% under-prediction in the local values.

Overall Smagorinsky and k -equation SGS models underpredict the profiles of Nu , but a secondary peak can also be observed in the predictions by these two models (Fig. 11). A comparison of the RANS results [36] with the present LES predictions and experimental results [3] of Nu is also shown in Fig. 11. It can be observed that the results of Nu by the RANS based SST $k-\omega$ turbulence model are highly over-predicted in the region of secondary peak due to the inability of this turbulence model to capture flow transition [36].

Fig. 14 Contours of normalized Q criterion for $H/B = 4$, $Re = 20,000$ and at different y^+ locations using dynamic k -equation model ($t^* = 1900$)

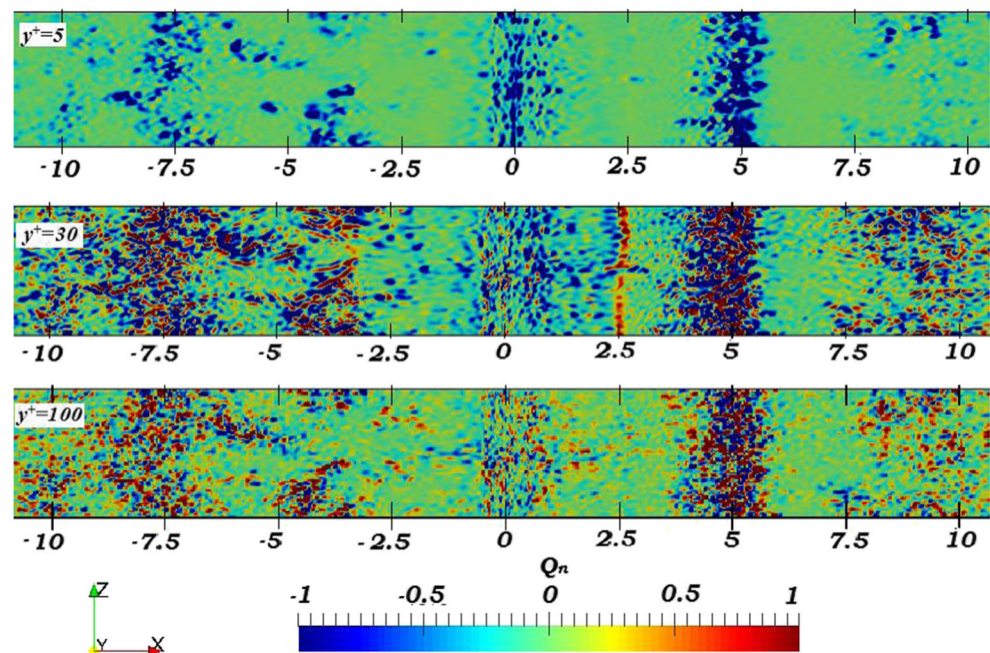


Fig. 12 shows the contours of (a) instantaneous velocity magnitude and (b) x -velocity for $H/B = 4$ and $Re = 20,000$ using the dynamic k -equation model. The shear-layer or potential core is deflected due to a low nozzle to plate spacing (Fig. 12). A growth of shear-layer can be observed in the streamwise direction. A typical wall jet development on the impingement plate can also be observed on either side of the jet central axis.

Figure 13 shows the contours of (a) time-averaged mean velocity and (b) turbulence kinetic energy for $H/B = 4$ and $Re = 20,000$ computed using the dynamic k -equation model. The present LES computations capture the spread rate of the mean velocity profiles. A stagnation point at $x/B = 0$ can be clearly observed, where the mean velocity magnitude is zero and the pressure will be maximum at this point. Further spread of wall jet can also be observed on either side of the jet (Fig. 13a). The stagnation region contains low turbulence kinetic energy and its values increase downstream due to a good mixing of flow (Fig. 13b). An augmentation in turbulence kinetic energy contours levels can be observed from $x/B = 2.5$ – 3 , due to a rise in turbulence level at downstream locations. The above-mentioned behaviour in this particular region can be related to the appearance of a secondary peak in Nusselt number (Fig. 11). Thus a secondary peak in Nusselt number is present due to an increased level of turbulence kinetic energy in the region close to $x/B = 3$.

Turbulence may not be seen as a random flow behaviour only but it can also be identified with spatially coherent and temporally developing vortical motions. Transport of turbulence characteristics is significantly influenced by coherent structures, which also help to identify physical appearance of turbulence. Figure 14 shows the contours of Q -criterion ($Q = 1/2(\Omega_{ij}\Omega_{ij} - S_{ij}S_{ij})$) in a x - z plane at various wall normal locations $y^+ = 5, 30$ and 100 from the impingement plate. The normalized Q -criterion defined as $Q_n = Q/Q_{max}$ is considered (here Ω denotes the vorticity magnitude and S the mean rate of strain tensor). Q criterion is a function object in OpenFOAM that calculates and stores the second invariant of the velocity gradient tensor. Turbulence increases with an increase in the value of y^+ (Fig. 14). The present LES is capable of capturing small scale dynamics. The magnitude of vorticity increases in the normal direction from the impingement plate and more turbulent structures can be observed. Larger and dense turbulent structures may be observed between $2.5 \leq x/B \leq 6$ at y^+ of 30 and 100 (Fig. 14) and this could be the reason for the presence of secondary peak in Nusselt number (Fig. 11).

6 Conclusions

Large eddy simulation was performed in the present study for a jet impingement on a heated surface for $H/B = 4$ and $Re = 20,000$ using four sub-grid stress (SGS) models, namely,

Smagorinsky, WALE (wall adapting local eddy viscosity), k -equation and dynamic k -equation. The Open source code OpenFOAM was used for computations. An implicit finite-volume method with a second-order accuracy in space and time was used. The mean streamwise velocity and r.m.s. velocity fluctuations along the stagnation and wall jet regions were computed and compared with the reported experimental results. The present results using WALE and dynamic k -equation models matched well with the experimental data, though velocity and turbulence profiles using the four LES SGS models followed the trends of the experimental results. The profiles of the normalized Nusselt number on the impingement wall were also computed by the four SGS models. WALE and dynamic k -equation models showed a good agreement with the experimental heat transfer data. A secondary peak in Nusselt number was observed using the four SGS models. It is shown that the present LES is capable of capturing small scale dynamics and WALE and dynamic k -equation SGS models performed well in complex flow regions.

Acknowledgements The authors acknowledge the HPC facility of Indian Institute of Technology Delhi for computational resources.

Compliance with ethical standards

Conflict of interest On behalf of all authors, the corresponding author states that there is no conflict of interest.

Publisher's Note Springer Nature remains neutral with regard to jurisdictional claims in published maps and institutional affiliations.

References

- Jambunathan K, Lai E, Moss MA, Button BL (1992) A review of heat transfer data for single circular jet impingement. *Int J Heat Fluid Flow* 13:106–115. [https://doi.org/10.1016/0142-727X\(92\)90017-4](https://doi.org/10.1016/0142-727X(92)90017-4)
- Shukla A, Dewan A (2017) Flow and thermal characteristics of jet impingement: comprehensive review. *Int J of Heat and Tech* 35: 153–166. <https://doi.org/10.18280/ijht.350121>
- Ashforth-Frost S, Jambunathan K, Whitney CF (1997) Velocity and turbulence characteristics of a semiconfined orthogonally impinging slot jet. *Exp Thermal Fluid Sci* 14:60–67. [https://doi.org/10.1016/S0894-1777\(96\)00112-4](https://doi.org/10.1016/S0894-1777(96)00112-4)
- Hoogendoorn CJ (1977) The effect of turbulence on heat transfer at a stagnation point. *Int J Heat Mass Transf* 20:1333–1338. [https://doi.org/10.1016/0017-9310\(77\)90029-1](https://doi.org/10.1016/0017-9310(77)90029-1)
- Lytle D, Webb BW (1994) Air jet impingement heat transfer at low nozzle-plate spacings. *Int J Heat Mass Transf* 31:1687–1697. [https://doi.org/10.1016/0017-9310\(94\)90059-0](https://doi.org/10.1016/0017-9310(94)90059-0)
- Zhe J, Modi V (2001) Near wall measurements for a turbulent impinging slot jet. *J Fluids Eng* 123:112–120. <https://doi.org/10.1115/1.1343085>
- O'Donovan TS, Murray DB (2007) Jet impingement heat transfer - Part I: Mean and root-mean-square heat transfer and velocity distributions. *Int J Heat Mass Transf* 50:3291–3301. <https://doi.org/10.1016/j.ijheatmasstransfer.2007.01.044>

8. Dutta R, Dewan A, Srinivasan B (2016) Large eddy simulation of turbulent slot jet impingement heat transfer at small nozzle-to-plate spacing. *Heat Transfer Eng* 37:1242–1251. <https://doi.org/10.1080/01457632.2015.1119592>
9. Dutta R, Dewan A, Srinivasan B (2013) Comparison of various integration to wall (ITW) RANS models for predicting turbulent slot jet impingement heat transfer. *Int J Heat Mass Transf* 65:750–764. <https://doi.org/10.1016/j.ijheatmasstransfer.2013.06.056>
10. Baydar E, Ozmen Y (2005) An experimental and numerical investigation on a confined impinging air jet at high Reynolds numbers. *Appl Therm Eng* 25:409–421. <https://doi.org/10.1016/j.althermaleng.2004.05.016>
11. Al-Sanea S (1992) A numerical study of the flow and heattransfer characteristics of an impinging laminar slot-jet including crossflow effects. *Int J Heat Mass Transf* 35:2501–2513. [https://doi.org/10.1016/0017-9310\(92\)90092-7](https://doi.org/10.1016/0017-9310(92)90092-7)
12. Yang Y-T, Tsai S-Y (2007) Numerical study of transient conjugate heat transfer of a turbulent impinging jet. *Int J Heat Mass Transf* 50:799–807. <https://doi.org/10.1016/j.ijheatmasstransfer.2006.08.022>
13. Viskanta R (1993) Heat transfer to impinging isothermal gas and flame jets. *Exp Thermal Fluid Sci* 6:111–134. [https://doi.org/10.1016/0894-1777\(93\)90022-B](https://doi.org/10.1016/0894-1777(93)90022-B)
14. Zuckerman N, Lior N (2005) Impingement heat transfer: correlations and numerical modeling. *J Heat Transf* 127:544–552. <https://doi.org/10.1115/1.1861921>
15. Olsson M, Fuchs L (1998) Large eddy simulations of a forced semiconfined circular impinging jet. *Phys Fluids* 10:476–486. <https://doi.org/10.1063/1.869535>
16. Cziesla T, Biswas G, Chattopadhyay H, Mitra NKK (2001) Large-eddy simulation of flow and heat transfer in an impinging slot jet. *Int J Heat Fluid Flow* 22:500–508. [https://doi.org/10.1016/S0142-727X\(01\)00105-9](https://doi.org/10.1016/S0142-727X(01)00105-9)
17. Beaubert F, Viazzo S (2002) Large eddy simulation of a plane impinging jet. *Cr Mecanique* 330:803–810. [https://doi.org/10.1016/S1631-0721\(02\)01537-1](https://doi.org/10.1016/S1631-0721(02)01537-1)
18. Beaubert F, Viazzo S (2003) Large eddy simulations of plane turbulent impinging jets at moderate Reynolds numbers. *Int J Heat Fluid Flow* 24:512–519. [https://doi.org/10.1016/S0142-727X\(03\)00045-6](https://doi.org/10.1016/S0142-727X(03)00045-6)
19. Icardi M, Gavi E, Marchisio DL, Olsen MG, Fox RO, Lakehal D (2011) Validation of LES predictions for turbulent flow in a confined impinging jets reactor. *Appl Math Model* 35:1591–1602. <https://doi.org/10.1016/j.apm.2010.09.035>
20. Kubacki S, Dick E (2010) Simulation of plane impinging jets with $k-\omega$ based hybrid RANS/LES models. *Int J Heat Fluid Flow* 31:862–878. <https://doi.org/10.1016/j.ijheatfluidflow.2010.04.011>
21. Heyerichs K, Pollard A (1996) Heat transfer in separated and impinging turbulent flows. *Int J Heat Mass Transf* 39:2385–2400. [https://doi.org/10.1016/0017-9310\(95\)00347-9](https://doi.org/10.1016/0017-9310(95)00347-9)
22. Jaramillo JE, Trias FX, Gorobets A, Pérez-Segarra CD, Oliva A (2012) DNS and RANS modelling of a turbulent plane impinging jet. *Int J Heat Mass Transf* 55:789–801. <https://doi.org/10.1016/j.ijheatmasstransfer.2011.10.031>
23. Kubacki S, Rokicki J, Dick E (2013) Hybrid RANS/LES computations of plane impinging jets with DES and PANS models. *Int J Heat Fluid Flow* 44:596–609. <https://doi.org/10.1016/j.ijheatfluidflow.2013.08.014>
24. Uddin N, Neumann SO, Weigand B (2013) LES simulations of an impinging jet: on the origin of the second peak in the Nusselt number distribution. *Int J Heat Mass Transf* 57:356–368. <https://doi.org/10.1016/j.ijheatmasstransfer.2012.10.052>
25. Gao S, Voke PR (1995) Large-eddy simulation of turbulent heat transport in enclosed impinging jets. *Int J Heat Fluid Flow* 16:349–356. [https://doi.org/10.1016/0142-727X\(95\)00050-Z](https://doi.org/10.1016/0142-727X(95)00050-Z)
26. Lodato G, Vervisch L, Domingo P (2009) A compressible wall-adapting similarity mixed model for large-eddy simulation of the impinging round jet. *Phys Fluids* 21:1–21. <https://doi.org/10.1063/1.3068761>
27. Dairay T, Fortuné V, Lamballais E, Brizzi LE (2014) LES of a turbulent jet impinging on a heated wall using high-order numerical schemes. *Int J Heat Fluid Flow* 50:177–187. <https://doi.org/10.1016/j.ijheatfluidflow.2014.08.001>
28. Sagaut P (2006) Large eddy simulation for incompressible flows: an introduction. Springer-Verlag, Berlin Heidelberg
29. Ferziger JH, Peric M (2002) Computational methods for fluid dynamics. Springer-Verlag, Berlin Heidelberg
30. Sohankar A, Davidson L, Norberg C (1999) A dynamic one-equation subgrid model for simulation of flow around a square cylinder. *Engineering Turbulence Modelling and Experiments* 4:227–236. <https://doi.org/10.1016/B978-008043328-8/50021-7>
31. Smagorinsky J (1963) General circulation experiments with the primitive equations: I The basic experiment*. *Mon Weather Rev* 91:99–164. [https://doi.org/10.1175/1520-0493\(1963\)091<0099:GCEWTP>2.3.CO;2](https://doi.org/10.1175/1520-0493(1963)091<0099:GCEWTP>2.3.CO;2)
32. Nicoud F, Ducros F (1999) Subgrid-scale stress modelling based on the square of the velocity gradient tensor. *Flow Turbul Combust* 62:183–200. <https://doi.org/10.1023/A:1009995426001>
33. Yoshizawa A (1986) Statistical theory for compressible turbulent shear flows, with the application to subgrid modeling. *Phys Fluids* 29(1958–1988):2152–2164. <https://doi.org/10.1063/1.865552>
34. Javed T, Md Mizanur R, Timos S, Ramesh KA (2015) One-equation sub-grid scale model with variable eddy viscosity coefficient. *Comput Fluids* 107:155–164. <https://doi.org/10.1016/j.compfluid.2014.10.014>
35. Kim W, Menon, S (1995) A new dynamic one-equation subgrid-scale model for large eddy simulation. In 33rd Aerospace Sciences Meeting and Exhibit, Reno, NV. <https://doi.org/10.2514/6.1995-356>
36. Shukla AK, Dewan A (2017) Convective heat transfer enhancement using slot jet impingement on a detached rib surface. *J Appl Fluid Mech* 10:1615–1627. <https://doi.org/10.18869/acadpub.jafm.73.243.27685>
37. Celik I, Cehreli ZN, Yavuz I (2005) Index of Resolution Quality for Large Eddy Simulations. *J Fluids Eng* 127:949–958. <https://doi.org/10.1115/1.1990201>
38. Nicoud F, Toda HB, Cabrit O, Bose S, Lee J (2011) Using singular values to build a subgrid-scale model for large eddy simulations. *Phys Fluids* 23. <https://doi.org/10.1063/1.3623274>